

# Spectroscopic Diagnostics of Enhanced Magnetron and Mesh Separation Effects in Cyclonic Atmospheric Pressure Plasma Surface Modification of Polyethylene Terephthalate

Hsiao-Ling Li<sup>1</sup> · Chun Huang<sup>1</sup>

Received: 27 April 2017 / Accepted: 4 August 2017 / Published online: 11 August 2017  
© Springer Science+Business Media, LLC 2017

**Abstract** The correlation of plasma surface modification consequence and the electron characteristics in plasma state with the enhanced magnetron source and metal mesh screen are studied by cyclonic-atmospheric-pressure plasma on polyethylene terephthalate (PET) surface. The contact angle measurement is employed to examine the plasma modified PET surface hydrophilicity. Optical emission spectroscopy is used to detect the electronic excitation temperature and electron density in cyclonic atmospheric pressure plasma. The electronic excitation temperature and the electron density are measured as the operational conditions of adding magnetron source and metal mesh separation. Boltzmann plot method is employed to estimate the electronic excitation temperature whereas electron density measurement by the Voigt profile. The results show that both electronic excitation temperature and electron density have similar trend i.e., both increasing with the enhanced magnetron source while decreasing trend is observed with passing through the metal mesh.

**Keywords** Cyclonic-atmospheric-pressure plasma · Surface modification · Electronic excitation temperature · Magnetron · Polyethylene terephthalate

## Introduction

The atmospheric-pressure plasma works have attracted the excessive attention for industrial claims including in thin film deposition, surface treatment, dry etching, and bacterial inactivation as a result of its high working rate and easy operation, which uses vacuum-free system [1]. In past decades, the numerous kinds of atmospheric-pressure plasmas have been established and utilized in various research fields [2]. In atmospheric-pressure plasmas, the initiating plasma is usually contaminated by electrode material or plasma

---

✉ Chun Huang  
chunhuang@saturn.yzu.edu.tw

<sup>1</sup> Department of Chemical Engineering and Materials Science, Yuan Ze University, 135 Yuan-Tung Road, Zhongli 32003, Taiwan

undesirable deposition [3]. Our plasma source, called cyclonic-atmospheric-pressure plasma, generates the chemically pure plasma because of no contact between the plasma and the electrode [4, 5]. This characteristic feature of this cyclonic plasma offers many motivating usages, such as polymeric membrane surface treatment, organicsilica thin film deposition, microorganism sterilization, and transparent conductive film cleaning. Up to now, only the surface modification efficiency of the cyclonic plasma operating at atmospheric pressure was examined [6]. The additional magnetron effects and the electron characteristics in cyclonic-atmospheric-pressure plasma were not well studied. Although several references have already published, the correlation of plasma surface modification effect and the electron characteristic of atmospheric pressure plasma are not fully understood.

The considerable awareness has been motivated for atmospheric pressure plasma surface modification processing on polymeric materials [7]. The plasma surface modification of polymers that involve chemical surface modification can persuade the chemical functionalization on polymer surface, in which new functional groups are created [8]. The atmospheric pressure plasma may obtain the noticeable issues for polymer surface treatment, though, due to the difficulties in minimization of unfavorable consequences, such as surface degradation [9]. Many species exist in the plasma state, including high-energy ions, electrons, ultraviolet photons, excited neutral species, reactive free radicals, and neutrals. The ion bombardment in plasma processing can easily cause the substantial ablation of polymer surface moieties, chain scission, and surface degradation. In order to better realize the atmospheric pressure plasma surface modification consequence, the effects of the magnetron source and the metal grid mesh screen in the glow discharge regime are studied. The additional magnetron was used to create the closed magnetic field to trap electrons, enhancing both the effectiveness of the initial ionization process of plasma and allowing plasma to be more easily generated at atmospheric pressure which reduces energy loss through gas collisions. However, the additional magnetron in the atmospheric pressure plasma might induce more high-energy particles such as ions to easily cause the possible surface degradation and unfavorable surface damages during plasma surface treatment. From this suggestion, the metal grid mesh screen was also conducted in study to figure out the influence of mesh screen in cyclonic atmospheric pressure plasma surface treatment. In this study, we chose to place a grid mesh at floating potential in cyclonic-atmospheric-pressure plasma in order to screen high-energy particles such as ions from the plasma glow discharge before interacting with the polymer samples and to study the separation effects of the metal grid mesh. Furthermore, the grid mesh was placed in the cyclonic-plasma system as floating potential, which is absent of an external electric field, and thus, no ion regeneration occurred between the mesh and the polymer sample. In this study, the enhanced magnetron effect and the mesh screen effect are parallel examined as different operational conditions.

By using optical emission spectroscopy (OES), the intensities of the photo-emitting plasma species were detected. Moreover, the changes of electronic excitation temperature and electron density during cyclonic-atmospheric-pressure plasma treatment on polyethylene terephthalate (PET) surface were studied. The transitions of electronic excitation temperature and electron density were detected by OES and the surface modification effects were examined by static contact angle measurement method. We present the results of the OES detection and plasma treated PET surface analysis of cyclonic-atmospheric-pressure plasma surface modification. The cyclonic plasma modified PET surface analysis was performed by contact angle analysis (CA), X-ray photoelectron spectroscopy (XPS), and atomic force microscope (AFM).

## Experimental Methods

The cyclonic-atmospheric-pressure plasma system shown in Fig. 1 was used to modify PET sample surface. This cyclonic plasma is based on two spinning capacitively coupled plasma jets which create a discharge cyclone to increase the surface treatment region. The double-pipe discharge jets used for the cyclonic-atmospheric-pressure plasma surface modification are similar to that reported in Refs. [5, 6]. This atmospheric-pressure plasma cyclone is obtained in a gas compartment with two capacitively coupled plasma jets placed a certain distance apart inside the gas compartment. A diffusing glow gradually fills the reactor region. It specifies that the luminous gas phase can also be stabilized by applying the enhanced cyclonic gas flow to the discharge as shown in Fig. 1. A detailed description and the operational procedures of cyclonic-atmospheric-pressure plasma system were reported in previous studies [4, 5]. Figure 2 shows the various operational conditions of cyclonic-atmospheric-pressure plasma surface modification on PET for determining the effects of the enhanced magnetron source and metal mesh screen. The plasma-surface-modification conditions included cyclonic plasma only, cyclonic plasma + enhanced magnetron source, cyclonic plasma + metal mesh, and cyclonic plasma + enhanced magnetron source + metal mesh for each experiment as shown in Fig. 2a–d. The treatment time was controlled in 60 s in all operational conditions in this study. Argon gas which used to create cyclonic-atmospheric-pressure plasma was an industrial grade with 99.995% purity and purchased from Min-Yang Gas Corporation. Poly (ethylene terephthalate) (PET) samples (0.5 mm thick) were supplied by Yo-Ho Corporation. Prior to use in experiment, each PET sample was rinsed with deionized water for 15 min by an ultrasonic cleaner, and dried completely in the air. The static contact angles of PET samples were measured by projecting an image of an automatic sessile droplet resting on a membrane surface with a Magic Droplet Model 100SB Video Contact Angle System (Sindatek Instruments

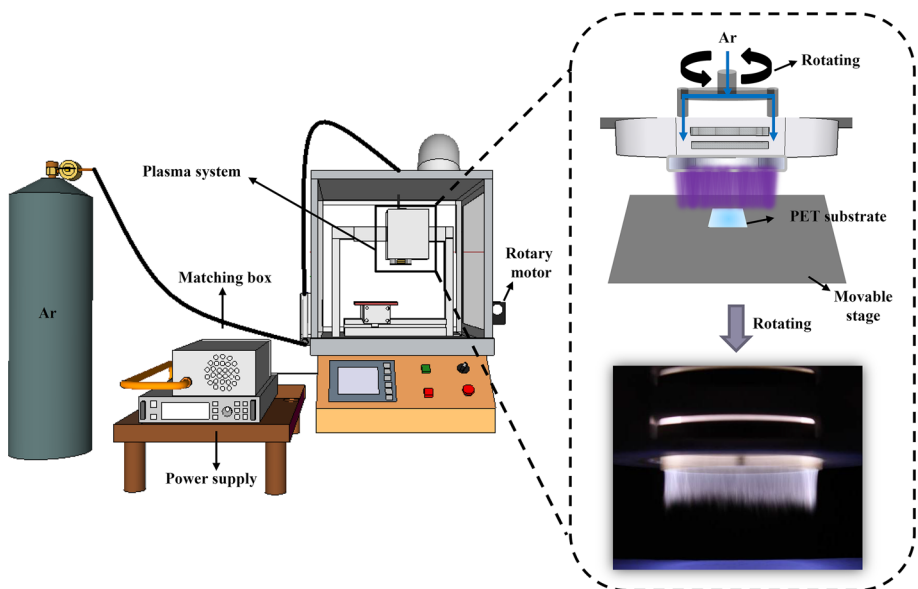


**Fig. 1** Schematic diagram of cyclonic atmospheric-pressure plasma

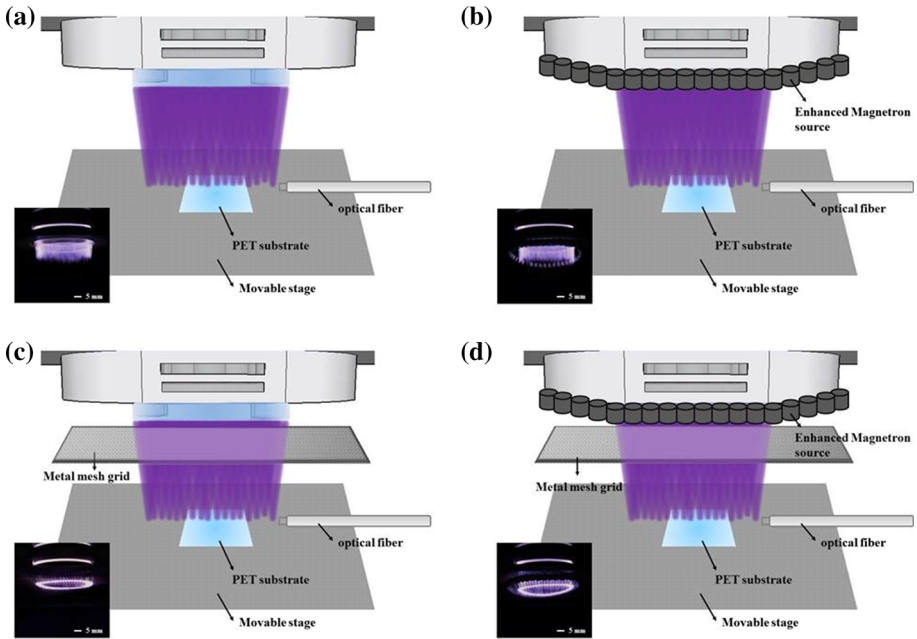


**Fig. 2** Schematic diagram of four plasma-surface-modification conditions. **a** Cyclonic plasma only, **b** cyclonic plasma + enhanced magnetron source, **c** cyclonic plasma + metal mesh and, **d** cyclonic plasma + enhanced magnetron source + metal mesh

Corporation, Taipei, Taiwan). The metal grid mesh was obtained from Jinji hardware store (Chungli, Taiwan) in sizes mesh 4. The metal grid mesh which was not electrically connected and placed it at floating potential in this study. To understand the nature of the surface change of the separator, the dispersion and polar interaction contributions to the surface energy of the materials were calculated using the Owens–Wendt model [10]. The liquids used for calculating the surface energies of the unmodified and atmospheric-pressure plasma-modified PET samples were water and di-iodomethane of known  $\gamma^p$  (polar component) and  $\gamma^d$  (disperse component). The surface energy of a solid ( $\gamma^s$ ) has two components, namely, a polar component and a disperse component. Both components contribute to the total surface energy:

$$\gamma_{LV}(1 + \cos \theta) = 2(\gamma_L^d \gamma_S^d)^{1/2} + 2(\gamma_L^p \gamma_S^p)^{1/2} \tag{1}$$

The electrical power provided to the discharge was calculated using the Lissajous diagram. Lissajous diagrams were used for understanding of the energy dissipated into the plasma in one cycle of the voltage. The area of the Lissajous diagram is equal to the one-cycle energy of the electrical discharge [11]. The discharge power is directly proportional to the area of the ellipse in the diagram, and can be calculated as:

$$P_{ave} = \frac{V_{max} \times I_{max}}{2} \cos \theta \tag{2}$$

The Lissajous diagrams of the discharge are shown in Fig. 3a and can also be used to determine the changes of the discharge characteristics for the plasma power input effect.

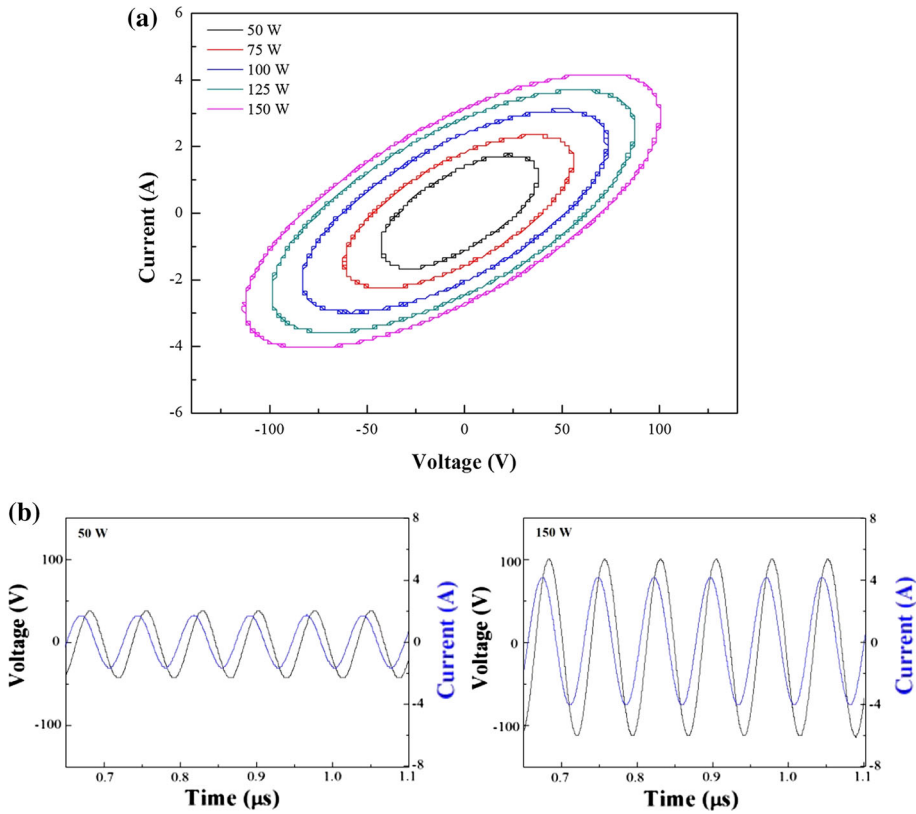


**Fig. 3** **a** Lissajous characteristic curves, **b** voltage and current waveforms from cyclonic atmospheric-pressure plasma with different powers

The shapes of the Lissajous diagrams containing multiple pulses are ellipses, and the discharge transition shows a region where the data points form a vertical line, corresponding to the peak in the current waveforms. Figure 3 shows that more than 90% of the input power was coupled into the cyclonic-atmospheric plasma when the input power was 150 W and the calculated power was 141 W. The voltage and discharge current were measured by a high voltage probe (Tektronix P6015A) and a current monitor (Pearson 4100) with a digital oscilloscope (Tektronix DPO2012). The applied voltage-current waveforms of cyclonic-atmospheric-pressure plasma for various plasma power inputs are shown in Fig. 3b. Obviously, the number of microdischarge pulses at a high RF plasma power is much greater than that at a lower RF plasma power. The number of microdischarges is directly related to the pollutant decomposition via low-temperature plasma. As can be seen in Fig. 3b, there is a small phase difference between discharge voltage and current in cyclonic atmospheric-pressure plasma. The current phase lag is as a result of the capacitive behavior of the plasma jet [12]. It actually comprises two electrodes forming a capacitor. On the other hand, the voltage and current peaks increase in cyclonic-atmospheric-pressure plasma, as can be seen in Fig. 3b. These changes can be attributed to the increasing breakdown voltage of the cyclonic atmospheric-pressure plasma of high plasma power input with respect to that of low plasma power. To detect the photo-emitting species,

and thus indirectly inspect the chemical composition of the glow discharge of the cyclonic-atmospheric-pressure plasma deposition system, OES was used as plasma diagnostic. OES consists of both the instrumentation and spectrum analysis software, which was supplied by Hong-Ming Technology, Inc. The observable spectral range was 250–950 nm with a resolution of 2 nm. An 1 m long fiber optic cable, coupled to an immobile width (50  $\mu\text{m}$ ) slit. The location of the optical fiber relative to the discharge was mounting on the tip of plasma cyclone contact with PET sample and the ambient air. In plasma parameters, electronic excitation temperature has a vital position because it gives the information of the collision process generating active species, density of active species, and reactions in the plasma state [13]. To calculate the electronic excitation temperature, it is assumed that the upper energy levels of the chosen atomic transitions are in local thermodynamic equilibrium that is; the population density of such levels follows the Boltzmann distribution. Taking into account the degeneracy of each atomic state, the population of a state can be determined from the OES spectrum. It is assumed that the electron energy distribution function (EEDF) for the free electrons in plasma is Maxwellian then we can write the approximate electron impact excitation rate from the ground state of argon as given by Drawing [14]. The line emission intensity related with the transition is proportional to the: number density of the atoms in the upper state, the probability of the transition and the energy of the emitted photon can be given by [15]

$$\ln\left(\frac{I_i\lambda_i}{g_iA_i}\right) = -\frac{E_i}{kT_e} + C \quad (3)$$

where  $I_i$  is observed emission intensity;  $\lambda_i$  is wavelength of the emission line;  $g_i$  is statistical weight of the level I;  $A_i$  is transition probability for spontaneous emission;  $E_i$  is excitation energy of the level I;  $k$  is Boltzmann constant,  $T_e$  is electronic excitation temperature;  $C$  is a constant and from the slope of the best linear fitting one can find the electron temperature. The electronic excitation temperature can be calculated from the slope of this line by using number of Ar-I lines. The spectroscopic data used for the measurement of excitation temperature are given in NiST database, as shown as Table 1 [16].

In this study, we used the methods based on OES to evaluate the electron density in the cyclonic-atmospheric-pressure plasma. Because of the numerous collisions among the particles in the atmospheric-pressure plasma discharge, the broadenings are represented as the different broadening mechanisms including in Stark, Van der Waals, Doppler, nature,

**Table 1** Relative parameters of the seven chosen Ar I lines

Wavelength (nm)	A ( $\text{s}^{-1}$ ) (transition probability)	E ( $\text{cm}^{-1}$ ) (upper state excited energy)	G (degeneracy)
696.5	6.39E+06	107,496.5	3
703	2.67E+06	119,683.1	5
706.7	3.80E+06	107,289.7	5
738.4	8.47E+06	107,289.7	5
750.4	4.45E+07	108,722.6	1
763.7	2.45E+07	106,237.6	5
772.42	1.17E+07	107,496.4	3

resonance, and instrument in the emission line [17, 18]. Each broadening mechanism results in a shift in the energy levels of the emitting atoms and the relative physical meaning of the broadenings is determined by the plasma operational factors such as power input and system pressure. In atmospheric pressure state, the resonance and natural broadening could be neglected [18]. Stark broadening  $\Delta\lambda_{stark}$  is directly related to electron density  $n_e$  and it can be represented as the following equation [19].

$$\Delta\lambda_{stark} = 1.96 \times 10^{-11} (n_e)^{2/3} \tag{4}$$

Van der Waals broadening  $\Delta\lambda_{van}$  is a vital broadening mechanism in high pressure plasmas and the full-widths at half-maximum (FWHM) profile can be calculated by the following equation [19, 20]

$$\Delta\lambda_{van} = 8.18 \times 10^{-12} \lambda^2 \left( \bar{\alpha} \times \overline{R^2} \right)^{\frac{2}{3}} (T_g/\mu)^{\frac{3}{10}} N \tag{5}$$

where  $\overline{R^2}$  is the difference of the squares of coordinate vectors of the upper and lower level,  $\lambda$  is the wavelength of the observed line in nm,  $\bar{\alpha}$  is the polarizability of perturbers interacting with the excited radiator in  $\text{cm}^3$ ,  $T_g$  is the temperature of the emitters (coincident with the gas temperature) in K,  $\mu$  is the atom-perturber reduced mass in a.m.u., and  $N$  is the density of perturbers in  $\text{cm}^{-3}$ . For an argon plasma at atmospheric pressure, when considering the van der Waals broadening of argon atomic lines ( $\mu = 19.97$  and  $\bar{\alpha} = 16.54 \times 10^{-25} \text{ cm}^3$ ), and the  $\overline{R^2} = 520$  [21].

$$\Delta\lambda_{van} = 4.4392 \times T_g^{-0.7} \tag{6}$$

Doppler broadening  $\Delta\lambda_{doppler}$  is caused by the random thermal motion of the emitting atoms and depends on the gas temperature  $T_g$  [20]. The approximate formula of FWHM profile is shown as below:

$$\Delta\lambda_{doppler} = 3.48 \times 10^{-4} T_g^{0.5} \tag{7}$$

where  $T_g$  is the gas temperature in Kelvin, and  $P$  is 1 atm. The gas temperature in this study was used as 338 K which was measured by thermocouple thermometer and the infrared thermal imaging. The instrumental broadening  $\Delta\lambda_{instrument}$  is referred 1.91 from the datasheet supported by Hong-Ming Technology in our study and the combination of the instrumental broadening and Doppler broadening are assumed to be Gaussian and the convolution can be presented by a Gaussian function with the FWHM by the expression [20].

$$\Delta\lambda_G^2 = \Delta\lambda_{doppler}^2 + \Delta\lambda_{instrument}^2 \tag{8}$$

And with the sum of Stark broadening and Van der Waals broadening, the Lorentz profiles can be expressed as  $\Delta\lambda_L$  and the convolution is also a Lorentz profile with the FWHM:

$$\Delta\lambda_L = \Delta\lambda_{stark} + \Delta\lambda_{van} \tag{9}$$

The combination of the Gaussian profile and Lorentz profile is a Voigt profile  $\Delta\lambda_v$  and the FWHM can be derived by [20]:

$$\Delta\lambda_V = \left[ \left( \frac{\Delta\lambda_L}{2} \right)^2 + \Delta\lambda_G^2 \right]^{\frac{1}{2}} + \frac{\Delta\lambda_L}{2} \quad (10)$$

The Voigt profile can be achieved by fitting the experimental values using Ar I 696.5 nm line profile and with a Voigt function gives the Voigt FWHM profile. From the previous equations, it can be organized as a one electron density equation from the correlation of the Voigt profile among the previous broadening mechanisms as follows:

$$n_e = \left[ \left( \frac{\Delta\lambda_V^2 - (1.21 \times 10^{-7} T_g + 3.6481)}{\Delta\lambda_V} - \frac{4.4392}{T_g^{0.7}} \right) \times \frac{1}{1.96 \times 10^{-11}} \right]^{\frac{3}{2}} \quad (11)$$

where  $\Delta\lambda_V$  is Voigt profile;  $\Delta n_e$  is electron density; P is 1 atm;  $T_g$  is gas temperature.

The surface morphology and the roughness of cyclonic-atmospheric-pressure-plasma-modified PET samples were examined by AFM, using a Veeco Dimension 5000 scanning probe microscopy. An arithmetic mean of surface roughness (root mean square, Rrms) was calculated from the roughness profile determined by AFM. A VG Scientific Microlab 310F system equipped with a Mg K $\alpha$  X-ray source (1253.6 eV) and a concentric hemispherical analyzer was used for surface analysis by X-ray photoelectron spectroscopy (XPS). Spectra were acquired with the angle between the direction of the emitted photoelectrons and the surface of PET samples equal to the take-off analysis angle of 70°.

## Results and Discussion

To detect the photo-emitting species, and thus indirectly observe the chemically reactive species of the cyclonic-atmospheric-pressure plasma, OES was used as a major plasma diagnostic in this study. OES analysis of the cyclonic-atmospheric-pressure plasma shows that the dominant argon emission lines are observed at 700–800 nm, as shown in Fig. 4.

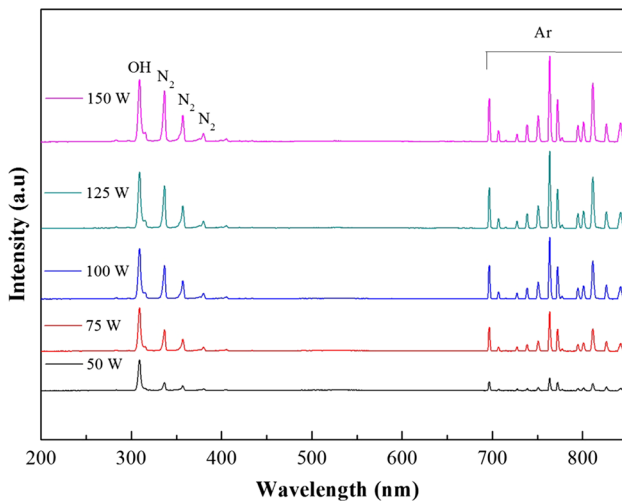


**Fig. 4** The optical emission spectrum from cyclonic-atmospheric-pressure plasma with argon gas. Plasma conditions: RF plasma power 50–150 W, Ar 10 slm



The emission lines of the molecular nitrogen bands, between 300 and 400 nm, are also seen in the OES spectra. It also shows the wide-scan spectra (300–800 nm) for various RF plasma power inputs to the cyclonic plasma state. It was also detected that, when more RF plasma power was introduced into the cyclonic plasma, the whole emission intensity, which was attributed to argon, was significantly enlarged, as shown in Fig. 4. From the OES observation, increasing the plasma power may enhance the surface modification results on account of the increased numbers of chemically reactive species in cyclonic-atmospheric-pressure plasma.

Recently, the interest for the spectroscopic diagnostics of atmospheric pressure plasma using spectral line is noticeably raised. One of the most widely used spectroscopic techniques for determining the electronic density results from the Stark broadening of measured spectral lines. The radioactive particles perturbation increase is caused by the electrical fields produced by the environmental electron and ions. In this method, the absolute intensities are not required, only the relative lines shape and width. For electron densities is  $10^{15} \text{ cm}^{-3}$ , the broadening is high, and standard spectrometers and monochromators are sufficient [21, 22]. Then, the full width at half maximum (FWHM) of these lines can be calculated using the electronic impact approximation and corrected by the important ionic quasi-static broadening; a shift in the line centers (usually toward higher wavelengths) is present far from the normal position [23]. Figure 5a shows the peak of argon at 696.5 nm line shape obtained by subtracting the background signal from the total spectrum. The measured line shape is well fitted with a Voigt profile of  $\text{FWHM} = 2.02\text{--}2.20 \text{ nm}$  as shown in Fig. 5a. Because the intensity of the  $\text{Ar}^*$  line is proportional to the population of rising RF plasma power inputs, the plasma power is dominated by emission from the cyclonic plasma. Therefore, the line-of-sight measurement provides, to good approximation, the electron density at the center line of the plasma. Deconvolution the Voigt profile return value of the FWHM Voigt profile (Gaussian profile and Lorentz profile). The difference between the measured FWHM of Lorentz profile and calculated the Van der Waals broadening gives the Stark broadening [19]. The electron density calculated from Gig-Card and GKS theory is shown in Fig. 5b and Table 2 [24]. The obtained electron density ranged  $0.12 \times 10^{15} \text{ cm}^{-3}$ – $3.59 \times 10^{15} \text{ cm}^{-3}$  depending on the absorbed plasma powers input and various operational conditions. Figure 5b also shows the increasing electron density with rising RF plasma power at all plasma-surface-modification conditions. It is clear from graph that the electron density increases with rising plasma power. It may be attributed to more collision of argon gas under higher plasma power input, and thus increase in electron collision frequency. This fact in turn provides enough energy for electrons to be accelerated in response of the applied field and; consequently an increase in the kinetic energy of electrons. The effects on the cyclonic-atmospheric-pressure plasmas and treatments of PET samples from the placement of a metal grid mesh in the plasma were also studied as shown in Fig. 5b and Table 2. The plasma-surface-modification conditions of cyclonic-atmospheric-pressure plasma included cyclonic plasma only, cyclonic plasma + enhanced magnetron source, cyclonic plasma + metal mesh, and cyclonic plasma + enhanced magnetron source + metal mesh. Table 2 shows the variation of electron density and the OES probe with respect to the additional magnetron and the metal mesh screen. For comparison, cyclonic plasma only and cyclonic plasma + enhanced magnetron source are also presented. The higher electron densities were obtained from cyclonic plasma + enhanced magnetron source as compared to cyclonic plasma only, to evaluate more frequently electron creation in the enhanced magnetron aid cyclonic plasma. From Table 2, both the enhanced magnetron and the

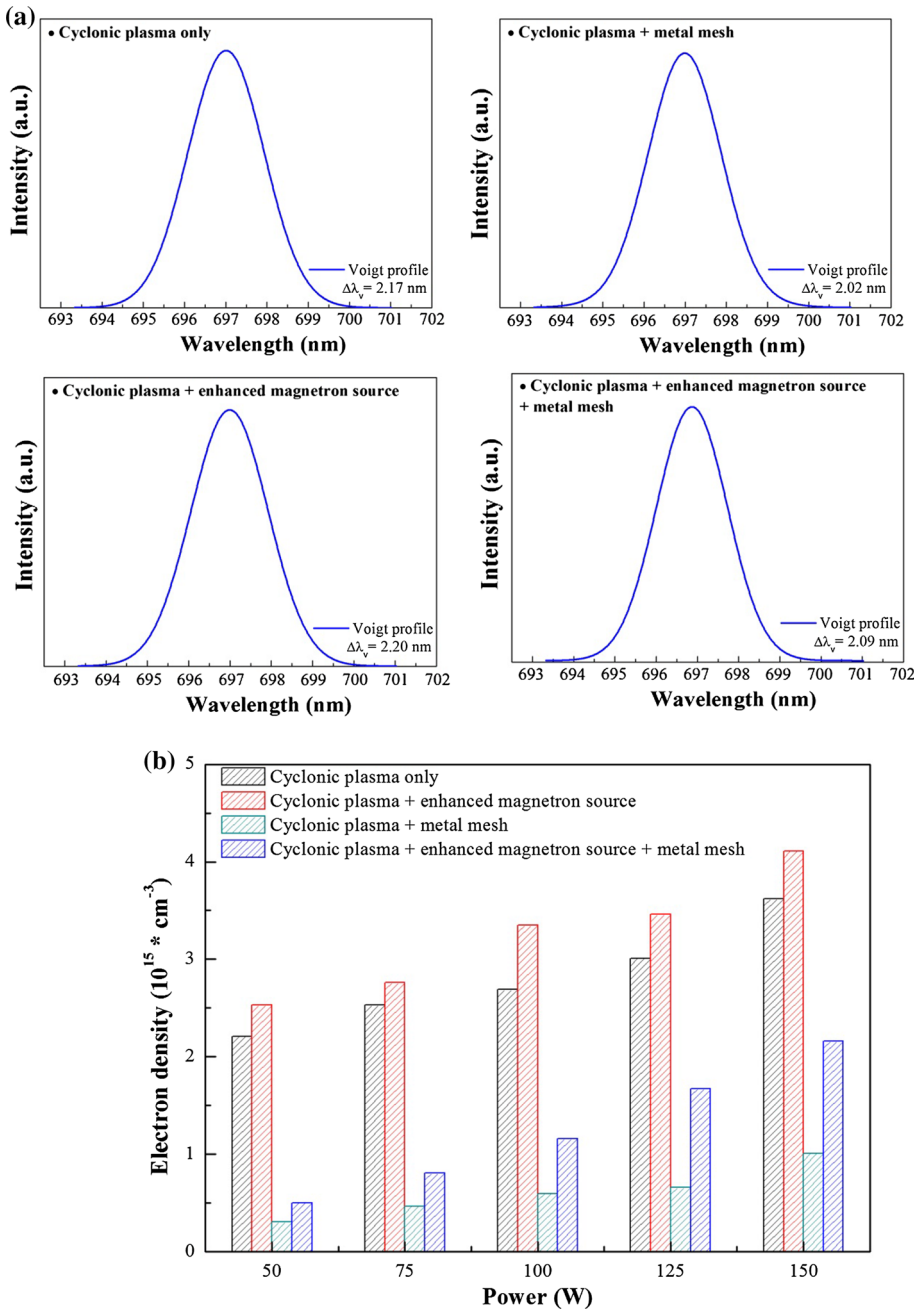


**Fig. 5** **a** The FWHM of argon peak at 696.5 nm and **b** variation of electron density at four plasma-surface-modification conditions. Plasma conditions: RF plasma power 50–150 W, Ar 10 slm

metal mesh screen effects for the modified PET surfaces are presented in cyclonic plasma + enhanced magnetron source + metal mesh. When a the metal mesh was placed in the configuration shown in Fig. 2d, however, the enhanced magnetron was

**Table 2** The value of the electron density for changing power at four plasma-surface-modification conditions

Power (W)	50	75	100	125	150
Cyclonic plasma only	$1.82 \times 10^{15} \text{ cm}^{-3}$	$2.12 \times 10^{15} \text{ cm}^{-3}$	$2.26 \times 10^{15} \text{ cm}^{-3}$	$2.55 \times 10^{15} \text{ cm}^{-3}$	$3.12 \times 10^{15} \text{ cm}^{-3}$
Cyclonic plasma + enhanced magnetron source	$2.13 \times 10^{15} \text{ cm}^{-3}$	$2.35 \times 10^{15} \text{ cm}^{-3}$	$2.91 \times 10^{15} \text{ cm}^{-3}$	$3 \times 10^{15} \text{ cm}^{-3}$	$3.59 \times 10^{15} \text{ cm}^{-3}$
Cyclonic plasma + metal mesh	$0.12 \times 10^{15} \text{ cm}^{-3}$	$0.25 \times 10^{15} \text{ cm}^{-3}$	$0.37 \times 10^{15} \text{ cm}^{-3}$	$0.42 \times 10^{15} \text{ cm}^{-3}$	$0.73 \times 10^{15} \text{ cm}^{-3}$
Cyclonic plasma + enhanced magnetron source + metal mesh	$0.3 \times 10^{15} \text{ cm}^{-3}$	$0.55 \times 10^{15} \text{ cm}^{-3}$	$0.86 \times 10^{15} \text{ cm}^{-3}$	$1.33 \times 10^{15} \text{ cm}^{-3}$	$1.77 \times 10^{15} \text{ cm}^{-3}$

also added, which slightly increased electron density compared to cyclonic plasma + metal mesh. Thus, the competition of the enhanced magnetron and metal mesh screen is not given. For cyclonic plasma + metal mesh, the lowest electron densities are presented in both Fig. 5b and Table 2.

For measurement of the kinetic temperature of free electrons, the electronic excitation temperature must be estimated [25]. This temperature is widely utilized in atmospheric pressure plasma and electron temperature measurement is based on this, the electronic excitation temperature determination because of their close relationship. Based on the suppositions, the electronic excitation temperature has been evaluated by Boltzmann technique, given by Refs. [26–28]. Figure 6 and Table 3 signify the electronic excitation temperature with rising RF plasma power at all plasma-surface-modification conditions that were obtained by Boltzmann plot assuming in local thermodynamic equilibrium condition. As shown in this Fig. 6, the electronic excitation temperature increases from 4674.19 to 7688.72 K with the rise in RF plasma power at all plasma-surface-modification conditions. Figure 6 also shows the variation of the electronic excitation temperature with growing RF plasma powers at different plasma-surface-modification conditions. It is clear from Fig. 6 that the electronic excitation temperature increases with plasma power while they rise with increase in current density. These facts can be explained as; with increase in plasma power the collision frequency of electrons with different chemically reactive species in the plasma enriches and electrons transfer their energy more frequently to the plasma species. Table 3 contains the electronic excitation temperature with rising RF plasma power at all plasma-surface-modification conditions. It is understandable from Table 3 that the mesh created a substantial disturbance in the cyclonic plasma and low electronic excitation temperature seems to be reflected by the mesh grid screen, even though the grid size was relatively large. The OES data indicates that the electronic excitation temperature was greatly reduced for all discharges by the placement of the mesh upstream from the PET sample in conditions of cyclonic plasma + metal mesh, and cyclonic plasma + enhanced magnetron source + metal mesh. In contrast, relatively high

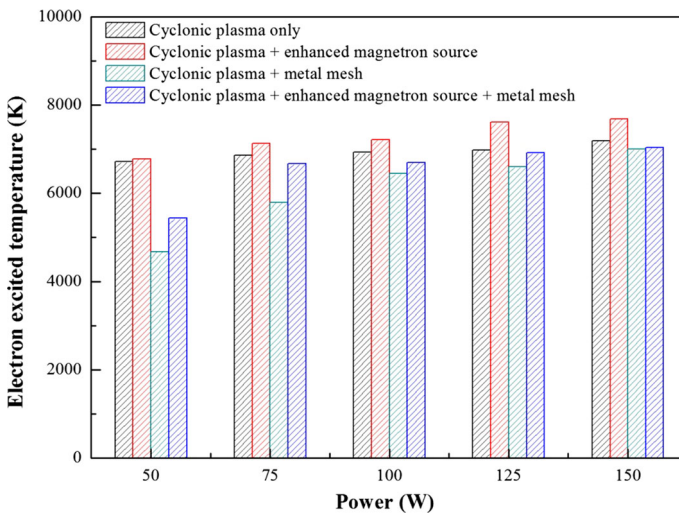


**Fig. 6** Variation of electron excited temperature at four plasma-surface-modification conditions. Plasma conditions: RF plasma power 50–150 W, Ar 10 slm

**Table 3** The value of the electron excited temperature for changing power at four plasma-surface-modification conditions

Power (W)	50 (K)	75 (K)	100 (K)	125 (K)	150 (K)
Cyclonic plasma only	6720.15	6862.3	6929.85	6982.49	7196.54
Cyclonic plasma + enhanced magnetron source	6782.71	7130.81	7216.47	7612.12	7688.72
Cyclonic plasma + metal mesh	4674.19	5793.16	6447.72	6603.13	6998.45
Cyclonic plasma + enhanced magnetron source + metal mesh	5433.46	6673.11	6699.15	6917.33	7042.64

electronic excitation temperature occurred in the cyclonic plasma without metal mesh screen in conditions of cyclonic plasma only and cyclonic plasma + enhanced magnetron source. The highest electronic excitation temperature obtained in cyclonic plasma + enhanced magnetron source confirms that the enhanced magnetron source effects on electron numbers as description in Table 2. Figure 7 shows the linear-fit plot by Boltzmann-plot method for the selected ArI lines at different operational conditions. The inverse of the slope of the linear fits give the electronic excitation temperature respectively. The electron excitation temperature can be estimated from the best linear fit of plot  $\ln(I_i \lambda_i / g_i A_i)$  versus

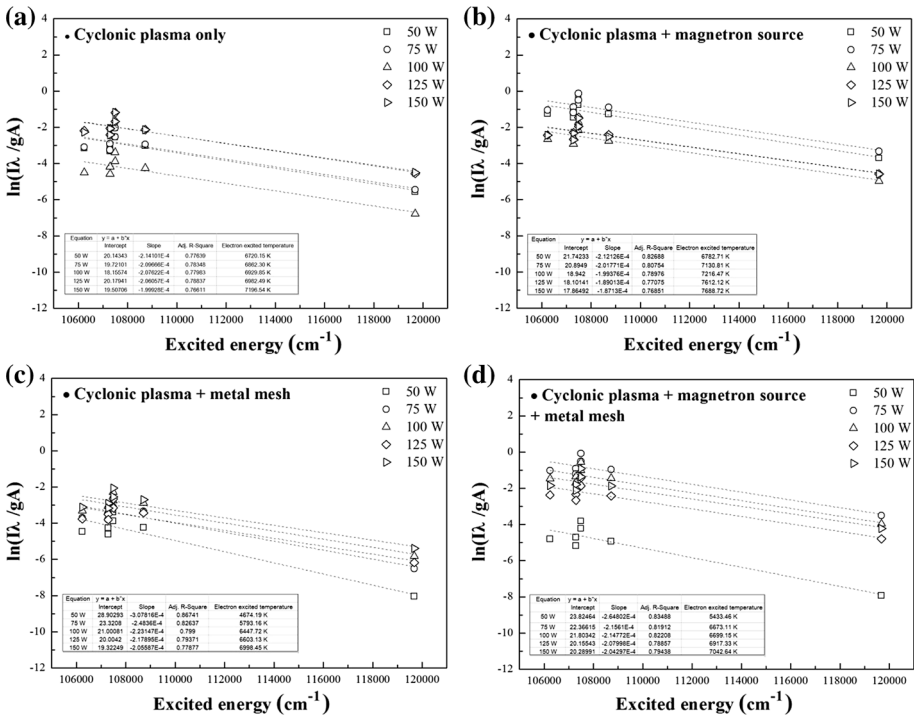


**Fig. 7** Linear regression of electron excited temperature **a** cyclonic plasma only, **b** cyclonic plasma + enhanced magnetron source, **c** cyclonic plasma + metal mesh and **d** cyclonic plasma + enhanced magnetron source + metal mesh. Plasma conditions: RF plasma power 50–150 W, Ar 10 slm

the excited energy ( $E_i$ ) shown in Fig. 7 [15]. Moreover it is also noted that the electron density and electronic excitation temperature acquire the comparable tendency.

Figure 8 shows the contact angle change of PET samples measured by static contact angle measurement method with diverse RF plasma power inputs and various conditions in cyclonic plasma surface modification. The relatively high surface free energies of all cyclonic plasma modified PET samples are shown in Fig. 8. The best wettability that was achieved without surface damage was in cyclonic plasma + enhanced magnetron source + metal mesh condition. The static contact angle data of the PET samples treated after the mesh in cyclonic plasma only and cyclonic plasma + enhanced magnetron source conditions reveal that the atmospheric pressure plasma surface modification were affected by the mesh screen, as indicated by relatively low wettability enhancement of the cyclonic plasma treated PET. The reactive species in cyclonic-atmospheric-pressure plasma, however, were reduced after the mesh. PET samples modified after the mesh in the cyclonic-atmospheric-pressure plasma, however, exhibited the wettability enhancement with less surface damage than those treated without using a mesh. The mesh setup in cyclonic plasma altered the discharge nature and a reduced amount of intensity of argon lines was observed during plasma surface modification on PET sample, which refers less energy transfer to the plasma state. Although a decrease in surface damage was observed on the treated PET samples by placement of the mesh screen in cyclonic-atmospheric-pressure plasma with/without the enhanced magnetron source, the wettability achieved was also greatly reduced. The contact angle measurement results of all cyclonic plasma surface modification on PET, shown in Fig. 8, however, showed a fewer diversity in static contact angle with various operational conditions. From this observation, therefore, the electron

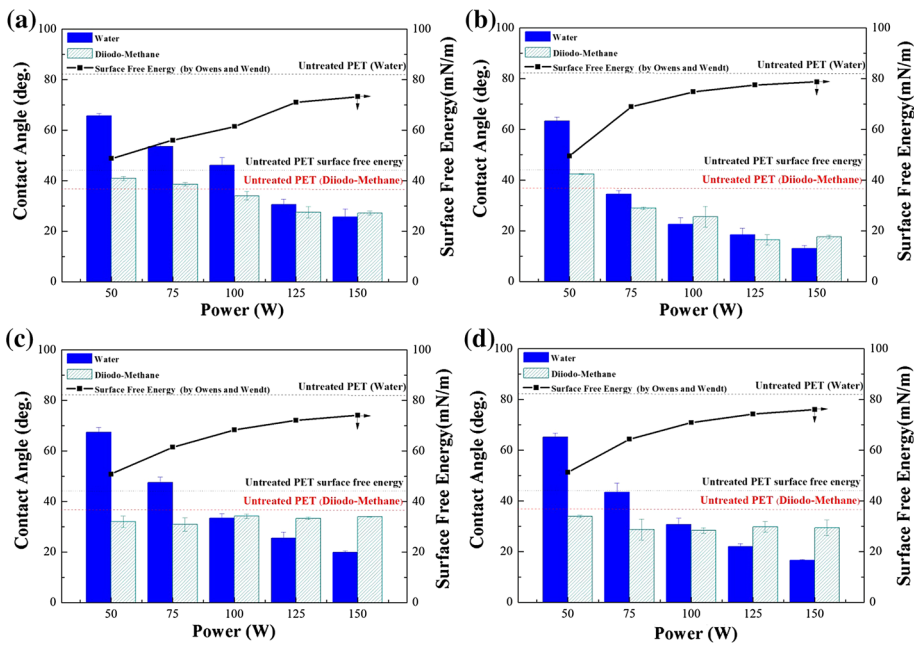


**Fig. 8** The contact angles and surface free energy for **a** cyclonic plasma only, **b** cyclonic plasma + enhanced magnetron source, **c** cyclonic plasma + metal mesh and **d** cyclonic plasma + enhanced magnetron source + metal mesh. Plasma conditions: RF plasma power 50–150 W, Ar 10 slm

evolution in cyclonic plasma state which is expressed by the electron density and electronic excitation temperature can be seen the minor key factor examined in the cyclonic plasma surface modification of PET samples. The possible reason is that in common plasmas; the group of high energy electrons play an important role in excitation of argon gas, but they are unable to effectively transfer their energy to the argon gases due to; inelastic collisions with the atoms [29]. When the enhanced magnetron and metal mesh were added to the cyclonic plasma, the collisions between excited argon metastable species with the external operational factors such as magnetron source and mesh screen occurred, resulting in an energy transfer to the reactive gas molecules. The direct outcome of such an energy transfer was non-production of new reactive plasma species from the added the enhanced magnetron and metal mesh. These plasma species thus formed also could react with the polymer surface, achieving surface modification of organic materials [30]. In the present study, cyclonic plasma without any additional enhanced magnetron and metal mesh as well as that with the addition of enhanced magnetron and metal mesh were used to modify the PET surfaces, and the resulting effects of plasma surface modification were studied.

Figure 9 shows the surface roughness of the cyclonic plasma modified PET samples with different operational conditions. The PET surface roughness was measured as the root-mean-square value obtained from the AFM analysis over an area of  $3 \times 3 \mu\text{m}^2$ . Figure 9a shows a bird's-eye view of relatively smooth surface of unmodified PET sample. It was also observed that the rougher surfaces of cyclonic plasma modified PET with different operational conditions. With adding magnetron source, the highest surface roughness was observed in Fig. 9c, consistent with the sequence of the electron density and electronic excitation temperature as shown in Figs. 5 and 6. It suggests that the grid mesh works to screen different plasma species such as high-energy ions, electrons, ultraviolet photons, excited neutral species, reactive free radicals, and neutral in this study. After penetrating the grid mesh, the endurance plasma species are guided into the similar flowing direction to PET sample which causes the isotropic surface features from AFM analysis. The substantial difference of surface morphological change from AFM analysis indicated that placing a floating mesh screen in the atmospheric pressure plasma inhibited PET surface damage from low-molecular-weight oxidized materials (LMWOM) formation, but did not further improve the surface hydrophilicity [31]. As a result, AFM shows that the surface morphological alteration of cyclonic plasma modified PET samples. It also refers that the surface morphological alteration and the electron evolution in cyclonic plasma state might dominate the wettability or surface hydrophilicity of PET during cyclonic plasma surface modification.

To study the major functional groups introduced into the PET surface by the cyclonic-atmospheric-pressure plasma, the XPS deconvolution analysis of C1s peaks was performed. The quantitative estimates of the atomic concentration in cyclonic plasma modified PET sample by XPS are summarized in Table 4. The percentage contributions of the C1s components of the cyclonic plasma modified PET surface, calculated from the C1s spectra, are shown in Fig. 10. As shown in Fig. 10a, the C1s spectrum of the unmodified PET surface contained a peak at 284.5 eV 285.9, and 287.3 corresponding to the C–C, –C–O, and C=O, groups [32]. The spectra of the cyclonic plasma modified PET surface (Figs. 10b–5e) also showed all peaks corresponding to the corresponding to the C–C, –C–O, and C=O, groups increased. At the same time, the peaks at 288.7 eV also appeared and increased in number, which are attributable to the O–C=O groups [33]. From these results, we propose that the cyclonic plasma cleaves the C–C bonds and introduces oxygen-containing functional groups into the molecular chain of the PET surface [34, 35]. The results suggest that these polar groups help increase the surface hydrophilicity of the PET.



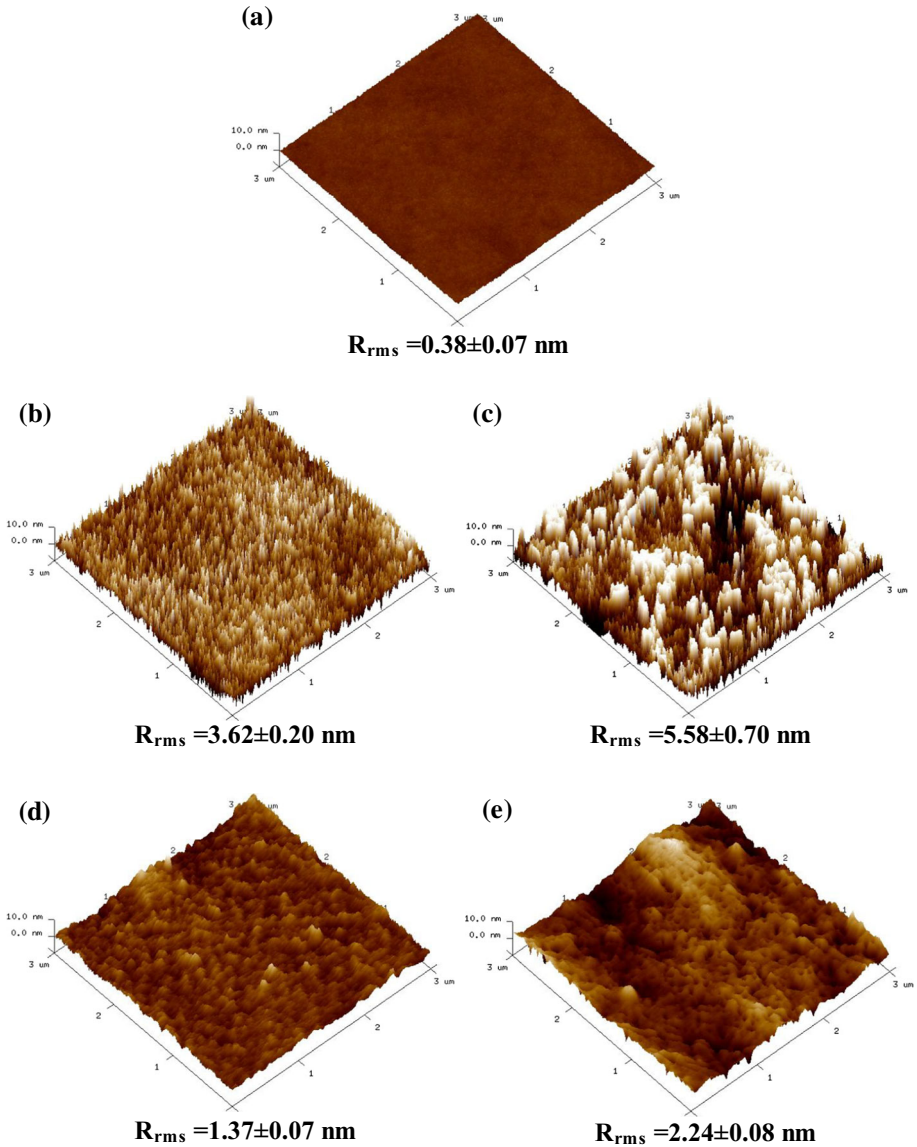


**Fig. 9** AFM images of atmospheric pressure plasma modified PET films at 150 W. **a** Untreated PET, **b** cyclonic plasma only, **c** cyclonic plasma + enhanced magnetron source, **d** cyclonic plasma + metal mesh and **e** cyclonic plasma + enhanced magnetron source + metal mesh. Plasma conditions: Ar 10 slm

It also found in Fig. 10 and Table 4 that the oxygen-containing groups from XPS analysis of cyclonic plasma modified PET samples in all conditions were increased and newly formed, but no significant difference was found from the data, as was consistent with the contact angle and surface free energy data shown in Fig. 8. From XPS analysis, it was concluded that the carbon content of the PET samples all decreased after cyclonic plasma treatment, the plasma modified PET samples obtain the similar characteristics after plasma



**Table 4** XPS chemical composition of cyclonic atmospheric pressure plasma modified PET films

Sample	Contribution of C <sub>1s</sub> components (%)				O–C=O
	C–C/C–H	C–C	C–O	C=O	
Untreated PET	73.98	5.98	10.73	1.42	7.88
Cyclonic plasma only	60.26	4.27	15.74	4.49	13.93
Cyclonic plasma + enhanced magnetron source	51.58	3.03	21.11	3.94	20.34
Cyclonic plasma + metal mesh	54.21	3.12	20.37	2.99	19.31
Cyclonic plasma + enhanced magnetron source + metal mesh	58.98	4.05	18.38	1.77	16.82

Plasma conditions: Ar 10 slm, RF plasma power 150 W

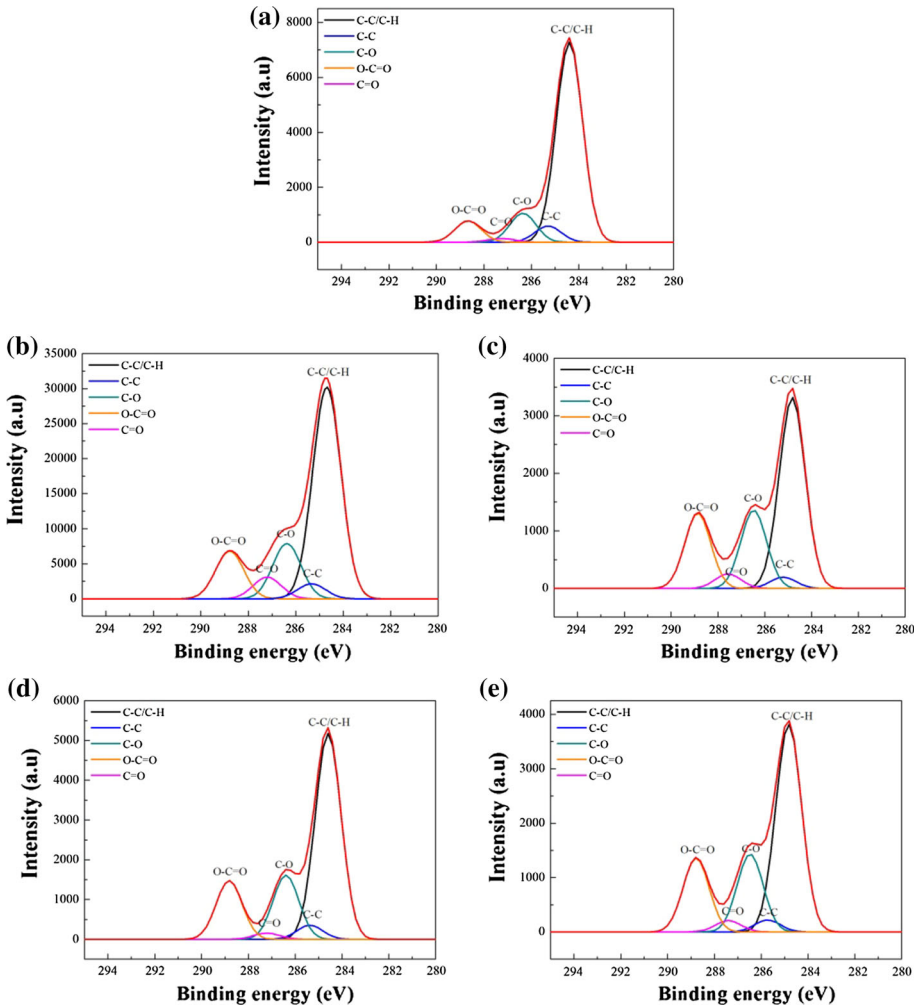


**Fig. 10** XPS C<sub>1s</sub> fitting of atmospheric pressure plasma modified PET films at 150 W. **a** Untreated PET, **b** cyclonic plasma only, **c** cyclonic plasma + enhanced magnetron source **d** cyclonic plasma + metal mesh and **e** cyclonic plasma + enhanced magnetron source + metal mesh. Plasma conditions: Ar 10 slm

surface treatment. These findings indicate an important message, which is that the plasma-polymer surface interaction and ion bombardment damage might not be key factors in atmospheric pressure plasma surface modification.

## Conclusions

In this study, the enhanced magnetron source and metal mesh screen was placed in cyclonic plasma discharge for PET surface modification to distinguish the effects of electrons in the atmospheric-pressure plasma from those of the other species, especially the electronically excited Ar species. OES is used to detect the electronic excitation temperature and the electron density in cyclonic-atmospheric-pressure plasma treatment on PET surface by various operational conditions of with/without the enhanced magnetron source and metal mesh. OES analysis indicates that the amount of electronically excited species in the cyclonic-atmospheric-pressure plasma was significantly influenced by adding magnetron source and passing through the grid mesh. The magnetron source was placed in cyclonic-plasma system to examine its enhancement effects on atmospheric-pressure plasma and on PET surface modification. It was found that the photo-emitting species were enlarged by the enhanced magnetron source. The increasing trend of both the electronic excitation temperature and electron density is observed for the operational condition of only enhanced magnetron source adding in cyclonic-atmospheric-pressure plasma surface modification. The metal mesh was also used in cyclonic plasma system to verify its separation effects on atmospheric-pressure plasma PET surface modification. The decrease of electronic excitation temperature and electron density is observed after the mesh placed in cyclonic plasma while small increase in adding the enhanced magnetron source is also noted with increasing electron density. The comparison of the electronic excitation temperature and the electron density and plasma modified PET wettability shows that the correlation between them exists in atmospheric-pressure plasma surface modification. It was found that the photo-emitting species were deflected by the screen and only weak glow was observed after the mesh. The static contact angle data also indicated that placing a the mesh screen in the cyclonic-atmospheric-pressure plasma inhibited PET surface damage, and enhance the surface wettability as effectively as it would without placing the mesh. Although it is possible that the mesh screen may have consumed high energy particles such as ions in cyclonic plasma, the reduction of the emission intensities of Ar species that reached the PET sample location was also favorable for wettability enhancement of PET. For PET samples modified in cyclonic plasma with enhanced magnetron source, the similar wettability enhancement and induced surface damage were observed in comparison with the plasma surface modification without a mesh.

**Acknowledgements** The authors appreciate the support of the Ministry of Science and Technology (MOST) under Grants 105-2221-E-155-073 and 106-2221-E-155-051.

## References

1. Kogelschatz U (2003) *Plasma Chem Plasma Process* 23(1):1–46
2. Ritts AC, Liu CH, Yu QS (2011) *Thin Solid Films* 519:4289–4824
3. De Geyter N, Morent R, Gengembre L, Leys C, Payen E, Van Vlierbergh S, Schacht E (2008) *Plasma Chem Plasma Process* 28:289–298

4. Huang C, Wu SY, Liu YC, Chang YC, Tsai CY (2011) *Jpn J Appl Phys* 50:01AH05-1–01AH05-5
5. Huang C, Lin HH, Li C (2015) *Plasma Chem Plasma Process* 35:1015–1028
6. Tseng YC, Li L, Huang C (2017) *Jpn J Appl Phys* 56:01AF03-1–01AF03-01-7
7. Hsu YW, Yang YJ, Wu CY, Hsu CC (2010) *Plasma Chem Plasma Process* 30(3):363–372
8. Francke KP, Rudolph R, Miessner H (2003) *Plasma Chem Plasma Process* 23(1):47–57
9. Gilliam M, Yu QS (2007) *J Appl Polym Sci* 105:360–372
10. Owens DK, Wendt RC (1969) *J Appl Polym Sci* 13:1741–1747
11. Chang YJ, Lin CH, Huang C (2016) *Jpn J Appl Phys* 55:01AB05-1–01AB05-6
12. Moravej M, Yang X, Barankin M, Penelon J, Babayan SE, Hicks RF (2006) *Plasma Sources Sci Technol* 15(2):204–210
13. Tsai JH, Hsu CM, Hsu CC (2013) *Plasma Chem Plasma Process* 33(6):1121–1135
14. Vacher D, Faure G, Andre P (2001) *Spectrochim Acta B* 56:309–330
15. Hao Z, Ji S, Liu H, Song Y (2014) *IEEE Trans Plasma Sci* 42:824–832
16. NIST Atomic Spectra Database. <http://physics.nist.gov/asd>
17. Qian MY, Ren CS, Wang DZ, Fan QQ, Nie QY, Wen XQ, Zhang JL (2012) *IEEE Trans Plasma Sci* 40:1134–1141
18. Liu W, Bernhardt J, Théberge F, Chin SL, Châteauneuf M, Dubois J (2007) *J Appl Phys* 102:033111-1–033111-4
19. Yubero C, Rodero A, Dimitrijevic MS, Gamero A, García MC (2017) *Spectrochim Acta B* 129:14–20
20. Gallagher TF (1999) *Phys Rep* 316:339–401
21. Ouyang Z, Surla V, Cho TS, Ruzic DN (2012) *IEEE Trans Plasma Sci* 40:3476–3481
22. Gomes AM, Saloum S, Sarrette JP (2004) *Plasma Chem Plasma Process* 24(2):239–259
23. Yubero C, Rodero A, Dimitrijevic MS, Gamero A, García MC (2017) *Spectrochim Acta Part B* 129:14–20
24. Yu L, Pierrot L, Laux CO, Kruger CH (2001) *Plasma Chem Plasma Process* 21:483–503
25. Hong YJ, Kwon GC, Cho G, Shin HM, Choi EH (2010) *IEEE Trans Plasma Sci* 38:1111–1116
26. Bakshi V, Kearney RJ (1989) *J Phys Chem Ref Data* 41:369–376
27. Capitelli M, Ferreira CM, Gordiets BF, Osipov R (2000) *Plasma Kinetics in Atmospheric Gases*. Springer, Berlin
28. Yalin AP, Laux CO, Kruger CH, Zare RN (2002) *Plasma Sources Sci. Technol.* 11:248–53
29. Gomes AM, Bacri J, Sarrette JP, Salon J (1992) *J Anal At Spectrosc* 7:1103–1109
30. Nam SH, Kim YJ (2001) *Bull Korean Chem Soc* 22-8:827–832
31. Yasuda H (2005) *Luminous chemical vapor deposition and interface engineering*. Marcel Dekker, NewYork
32. Gilliam M, Farhat S, Zand A, Magyar M, Garner G (2014) *Plasma Process Polym* 11:1037–1043
33. Morent R, Geyer ND, Vlierberghe SV, Beaurain A, Dubruel P, Payen E (2011) *Prog Org Coat* 70:336–341
34. Gonzalez E II, Barankin MD, Guschl PC, Hicks RF (2008) *Langmuir* 24:12636–12643
35. Gilliam M, Ritts A, Yu QS (2010) *J Appl Polym Sci* 118(2):805–817